Which phonons induce non-equilibrium superconductivity in $YBa_2Cu_3O_{6.5}$?

B. Liu[1], M. Först[1], M. Fechner[1], D. Nicoletti[1], J. Porras[3], B. Keimer[3], A. Cavalleri[1,2]

[1]*Max Planck Institute for the Structure and Dynamics of Matter, Hamburg, Germany.*
[2]*Department of Physics, University of Oxford, Clarendon Laboratory, Oxford, UK*
[3]*Max Planck Institute for Solid State Research, Stuttgart, Germany.*

Terahertz-frequency excitation in the cuprates has been shown to induce non-equilibrium superconducting correlations above the thermodynamic transition temperature, T_C. In $YBa_2Cu_3O_{6+x}$, this phenomenon has been associated with the nonlinear excitation of certain lattice modes. However, to date it has not been possible to tune the pump wavelength widely to systematically compare the effect of different modes. Aided by a newly developed optical device, we measured the response of $YBa_2Cu_3O_{6.5}$ to tuneable driving between 3 and 24 THz, covering all phonon resonances. We show that superconductivity is enhanced *only* for excitation of the 16.4 THz and 19.2 THz vibrational modes that modulate the position of apical oxygen atoms along the *c* axis. Other phonons only enhance the dissipation. We argue here that not only the average deformation of the lattice, but also a direct coupling between lattice vibrations and the electronic structure of the CuO_2 planes should contribute to enhanced non-equilibrium superconductivity.

The equilibrium superconducting state of high-T_C cuprates manifests itself in a number of characteristic features in the terahertz-frequency optical response. In Figure 1, we report selected optical properties measured in $YBa_2Cu_3O_{6.5}$ above and below the superconducting transition temperature, T_C.

As the temperature is lowered from 100 K (black curve, $T \gg T_C \simeq 52$ K) to 10 K (red curve, $T \ll T_C$), the real part of the *c*-axis optical conductivity, $\sigma_1(\omega)$, evolves from that of a semiconductor with thermally-activated carriers to a gapped spectrum (see Fig. 1b.1). Simultaneously, a zero-frequency δ-peak emerges, indicative of dissipation-less DC transport. This peak is not seen directly in $\sigma_1(\omega)$, but is reflected in a $\sim 1/\omega$ divergence in the imaginary conductivity, $\sigma_2(\omega)$ (Fig. 1b.2). Correspondingly, in the superconducting state the optical reflectivity evidences a sharp edge, the Josephson Plasma Resonance (JPR), which develops at $\omega \simeq \omega_{JPR} \simeq$ 30 cm^{-1} (Fig. 1b.3) [1,2,3].

A number of recent pump-probe experiments have shown that these same optical signatures of coherence (Fig. 1b, red curves) could be recreated transiently in $YBa_2Cu_3O_{6+x}$ for base temperatures $T \gg T_C$ by optical excitation near 20 THz [4,5,6]. Measurements of the transient atomic structure with femtoscond x-ray diffraction revealed that the nonlinear lattice dynamics launched by the 20 THz driving [7,8] induce an average structural deformation [9] in $YBa_2Cu_3O_{6.5}$. It was reasoned that such a structure may favor higher temperature superconductivity [9].

However, all these phenomena have not been systematically checked for excitation of different lattice modes, as no optical device could selectively drive these materials throughout the terahertz spectrum.

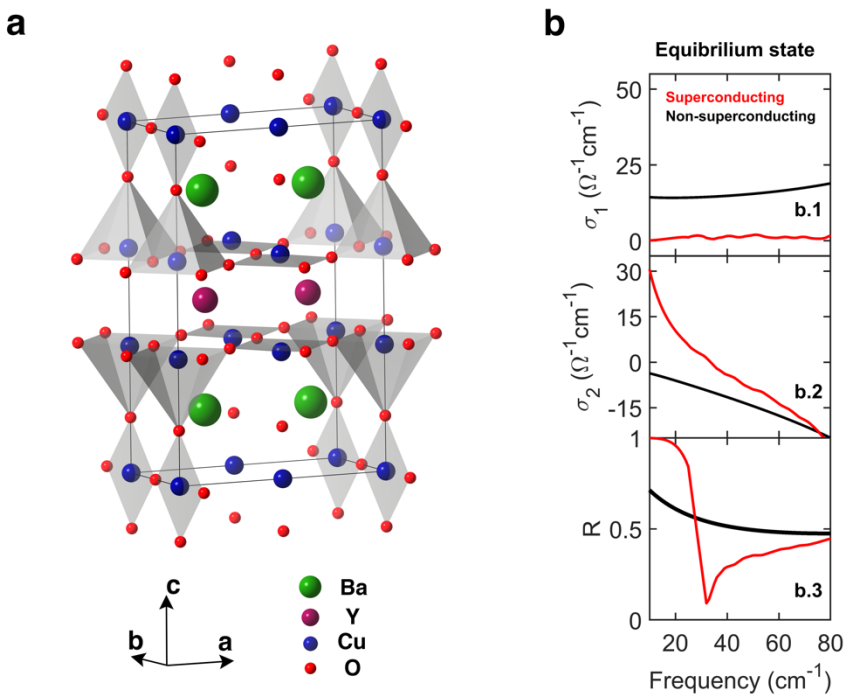

FIG. 1. Crystal structure and equilibrium THz optical properties of $YBa_2Cu_3O_{6.5}$. (a) Crystallographic unit cell of orthorhombic $YBa_2Cu_3O_{6.5}$. Bilayers of conducting CuO_2 planes, stacked along the *c* direction, form Josephson junctions in the superconducting state. (b) *c*-axis THz-frequency optical properties in the equilibrium superconducting ($T < T_C$, red curves) and normal ($T > T_C$, black curves) state. The real, $\sigma_1(\omega)$, and imaginary part, $\sigma_2(\omega)$, of the optical conductivity are displayed along with the normal-incidence reflectivity, $R(\omega)$ (same data as those reported in Refs. [4,5,6]).

Here, we make use of a new optical parametric amplifier [10] based on difference frequency mixing of chirped near infrared pulses [11] in organic crystals (see Supplemental Material [12]), to selectively drive $YBa_2Cu_3O_{6.5}$ at all frequencies throughout the terahertz electromagnetic spectrum (3 - 24 THz; 100 - 800 cm^{-1}). The relevant pump frequency range is displayed in Fig. 2b, which reports the equilibrium broadband *c*-axis optical conductivity, $\sigma_1(\omega)$, at $T = 100\ K$ [2,3].

In the first set of experiments, summarized in Fig. 2c-2d, we expanded the results reported in Refs. [4,5,6]. The excitation pulses were centered at 19.2 THz (640 cm^{-1}), which corresponds to apical oxygen distortions at the oxygen deficient chains. These experiments were first performed with the same broadband ~4-THz-wide pulses used in Refs. [4,5,6], and then, for comparison, with the newly available ~1-THz spectral

bandwidth (narrowband). These pump pulses were focused onto the sample at a fluence of ~8 mJ/cm^2. Note that in the narrowband experiments the pulses were four times longer than in the broadband experiments. As these two measurements used the same pump fluence, the peak electric fields were of 6 and 3 MV/cm for broadband (short pulse) and narrowband (long pulse) excitation, respectively.

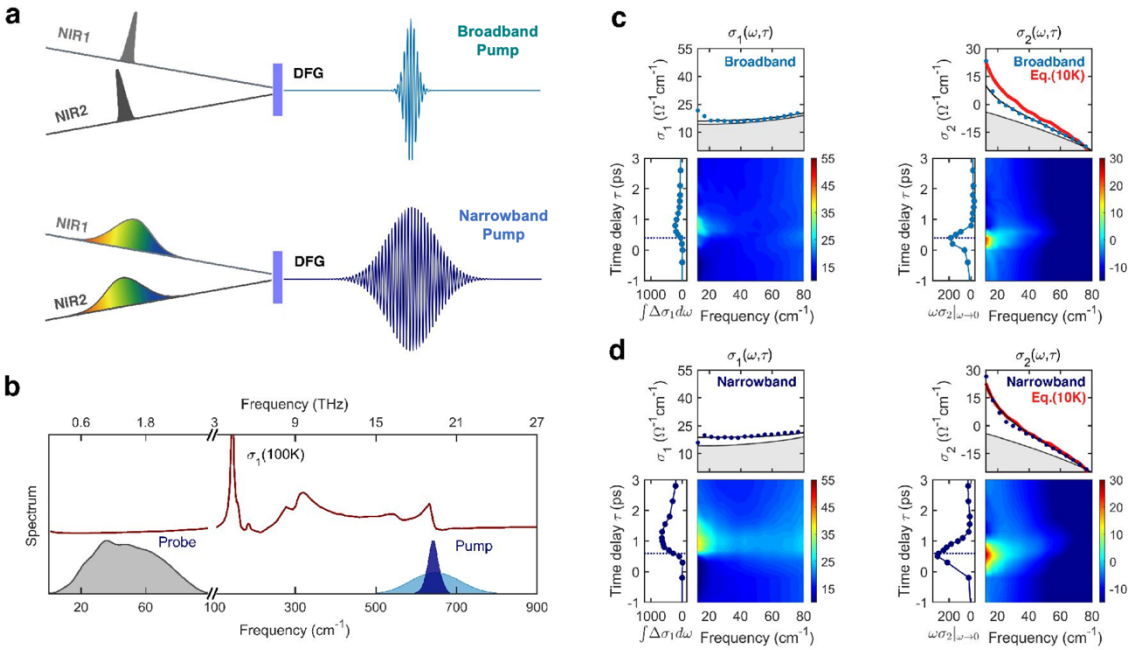

FIG. 2. Transient *c*-axis optical conductivity induced by apical oxygen excitation above T_C. (a) Schematics of the generation processes for broadband and narrowband excitation pulses. The signal outputs (NIR1 and NIR2) of two parallel optical parametric amplifiers were directly sent to a nonlinear crystal to generate broadband pump pulses (relative bandwidth $\Delta\nu/\nu \sim 20\%$) in a difference frequency generation (DFG) process. For narrowband generation ($\Delta\nu/\nu < 10\%$), the two signal outputs were linearly chirped before the DFG process (see Supplemental Material [12] for further details). (b) Equilibrium *c*-axis optical conductivity, $\sigma_1(\omega)$, of $YB_2Cu_3O_{6.5}$ at 100 K ($T > T_C$, red solid line), along with the frequency spectra of THz probe (grey), broadband pump (light blue), and 19.2 THz narrowband pump (dark blue) pulses. (c) Color plots: Frequency- and time-delay-dependent complex optical conductivity measured after broadband excitation at T = 100 K. Upper panels: corresponding $\sigma_1(\omega)$ and $\sigma_2(\omega)$ line cuts displayed at equilibrium (grey lines) and at the peak of the coherent response ($\tau \simeq 0.5$ ps time delay, blue circles). Black lines are fits to the transient spectra with a model describing the response of a Josephson plasma (see Supplemental Material [12] for details on the fitting procedure). For comparison, we also report the equilibrium $\sigma_2(\omega)$ measured in the superconducting state at T = 10 K (red line). Side panels: Frequency-integrated dissipative ($\int \Delta\sigma_1(\omega)d\omega$) and coherent ($\omega\sigma_2(\omega)|_{\omega\to0}$) responses, as a function of pump-probe time delay. The delay corresponding to the spectra reported in the upper panels ($\tau \simeq 0.5$ ps) is indicated by a dashed line. (d) Same quantities as in (c), measured for narrowband excitation at 19.2 THz.

As already discussed in Refs. [4,5,6], the transient *c*-axis optical properties were interrogated between ~15 and 80 cm^{-1} by reflecting a second terahertz probe pulse generated by optical rectification in a nonlinear crystal. The electric field of these pulses was then electro-optically sampled (Fig. 2b, grey spectrum) for different pump-probe time delays (see Supplemental Material [12] for further details).

Figures 2c-2d report the photoinduced changes in the complex optical conductivity at $T = 100\ K \gg T_C$, as a function of frequency and pump-probe time delay (color plots). Both excitation schemes induced qualitatively similar optical properties, with a significant increase in the imaginary conductivity, $\sigma_2(\omega)$, which became positive and exhibited a superconducting-like $\sim 1/\omega$ divergence for $\omega \to 0$. This is particularly evident in the frequency spectra measured at the peak of the signal, displayed above the color plots in Figs. 2c-2d (right panels). In these line cuts, the transient $\sigma_2(\omega)$ measured at $\tau \simeq 0.5$ ps after excitation (blue dots) is superimposed with the equilibrium $\sigma_2(\omega)$ at $T < T_C$ (red line, for comparison). Strikingly, for narrowband excitation at $T = 100$ K we observed exactly the same $\sigma_2(\omega)$ spectrum measured in the equilibrium superconducting state (T = 5 K $\ll$ T_C = 52 K) in the same sample.

The photo-induced dynamics at longer time delays ($\tau \gtrsim 1$ ps) was characterized instead by decoherence and increased dissipation, as observed in the real part of the optical conductivity, $\sigma_1(\omega)$ (Figs. 2c-2d, left panels).

On the left hand side of each panel, we plot two frequency-integrated quantitites as a function of time delay: $\omega\sigma_2(\omega)|_{\omega\to 0}$, which in an equilibrium superconductor is proportional to the superfluid density, and $\int \Delta\sigma_1(\omega)d\omega$, which is a reporter of dissipation and quasiparticle heating. For both broadband and narrowband excitation, it is evident that the dissipative part of the optical response ($\int \Delta\sigma_1(\omega)d\omega$, left panels

in Figs. 2b-2c), increases only after the superconducting component, $\omega\sigma_2(\omega)|_{\omega\to 0}$, has relaxed (right panels in Figs. 2b-2c).

Figure 3 reports a more comprehensive set of experiments similar to the ones reported in Fig. 2, obtained by tuning the pump pulse frequency widely throughout the excitation spectrum. Four selected results are displayed, corresponding to resonant narrowband excitation of four different phonon modes (see Supplemental Material [12] for additional data sets). The data reported in Fig. 2 ($\omega_{pump} = 19.2$ THz = 640 cm^{-1}) is shown alongside the results for excitations at $\omega_{pump} = 16.4$ THz = 550 cm^{-1}, $\omega_{pump} = 10.1$ THz = 340 cm^{-1}, and $\omega_{pump} = 4.2$ THz = 140 cm^{-1}, all driven by maintaining constant 3 MV/cm field strength.

The atomic displacements of these vibrational modes are displayed in Fig. 3a. The 4.2 THz mode involves motions of the barium atoms and of the apical oxygens. The 10.1 THz mode is associated with a planar Cu-O buckling motion, while the 16.4 THz and the 19.2 THz modes involve almost exclusively oscillations of the apical oxygen atoms on oxygen-rich and oxygen-deficient Cu-O chains, respectively.

The four pump-probe experiments reported in Fig. 3b-3c, where we display selected spectra taken at the peak of the coherent response (at time delay $\tau \simeq 0.5$ ps), show that driving at the two highest frequencies modes (16.4 THz and 19.2 THz) induces a superconducting-like response ($\sigma_2(\omega) \propto 1/\omega$), for which the transient complex conductivity is fitted by a model describing the optical response of a Josephson plasma. On the other hand, excitation of the two low-frequency modes (4.2 THz and 10.1 THz) causes only a moderate increase in dissipation and no superconducting component. This observation could be well reproduced, for all time delays, by a Drude-Lorentz model for normal conductors (see Supplemental Material [12] for details on the fitting procedure).

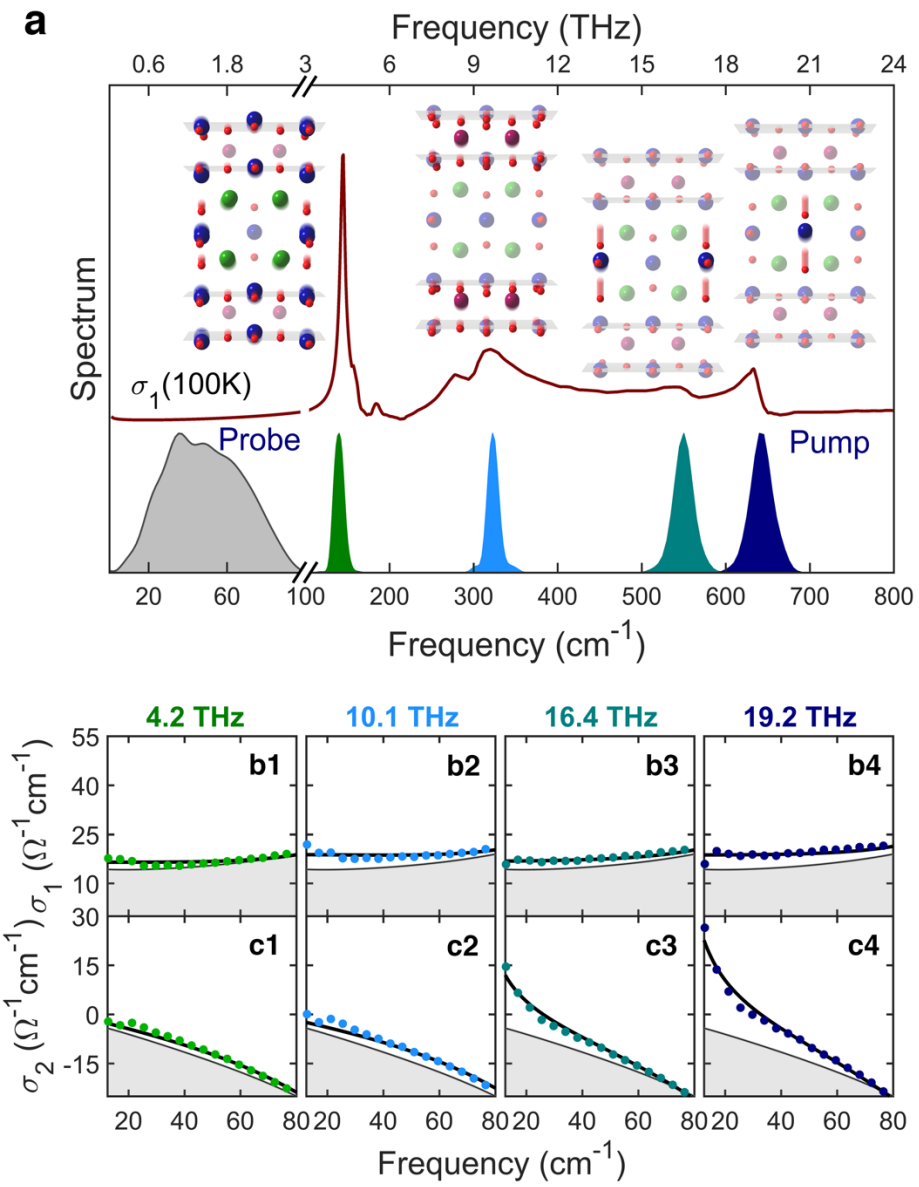

FIG. 3. Transient *c*-axis optical response induced by mode-selective phonon excitations above T_C. (a) Equilibrium *c*-axis optical conductivity, $\sigma_1(\omega)$, of $YB_2Cu_3O_{6.5}$ at 100 K ($T > T_C$, red solid line), along with the frequency spectra of THz probe (grey) and of different narrowband pump pulses, tuned to be resonant with four different optical phonons at 4.2 THz, 10.1 THz, 16.4 THz, and 19.2 THz. The insets sketch the atomic motions related to each of these modes, with CuO_2 layers highlighted in grey and transparency applied to quasi-stationary atoms. (b,c) Complex optical conductivity, $\sigma_1(\omega) + i\sigma_2(\omega)$, measured before (grey lines) and at $\tau \simeq 0.5$ ps time delay (colored circles) after resonant stimulation of the phonon modes shown in (a) with ~3 MV/cm peak electric fields. The black solid lines are fits to the transient spectra performed with either a simple Drude-Lorentz model for normal conductors (b1, b2, c1, c2) or a model describing the response of a Josephson plasma (b3, b4, c3, c4) (see Supplemental Material [12] for more details on the fitting procedure).

The same experiments as those reported in Fig. 3 were systematically repeated for 42 pump wavelengths. In Figure 4, for each pump frequency we report the results of the analysis of the transient optical properties at the time delay corresponding to the peak

of the coherent response. In the topmost panel, we show the total, spectrally integrated probe signal, that is the modulus of the complex optical conductivity, for each of the corresponding pump wavelengths reported on the horizontal axis. In the middle plot we report only the dissipative component of the signal ($\int \Delta\sigma_1(\omega)d\omega$), and in the lower plot only the superconducting contribution, $\omega\sigma_2(\omega)|_{\omega\to 0}$ (see Supplemental Material [12] for extended data sets).

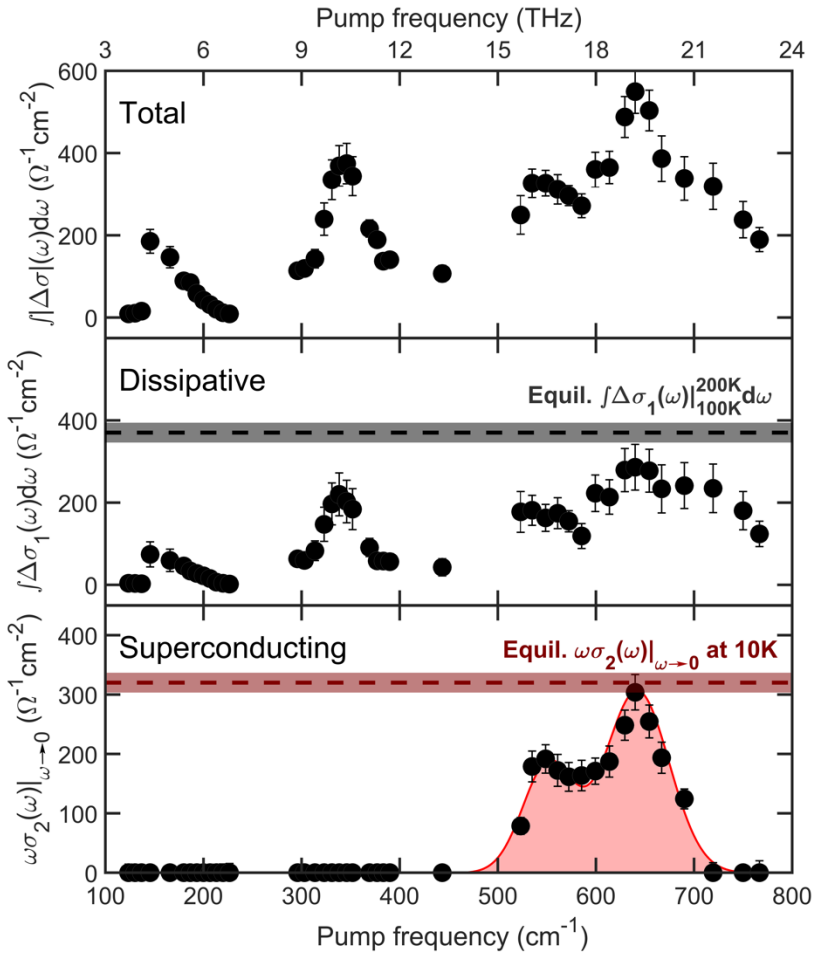

FIG. 4. Evolution of the photo-induced response as a function of excitation frequency. Distinct quantities, extracted from the transient optical conductivity at $\tau \simeq 0.5$ ps time delay, are displayed as a function narrowband excitation frequency: (a) The total, frequency integrated change in optical conductivity $\int|\Delta\sigma(\omega)|d\omega$, (b) the frequency integrated dissipative response, $\int\Delta\sigma_1(\omega)d\omega$, and (c) the superconducting response represented by the low-frequency limit $\omega\sigma_2(\omega)|_{\omega\to 0}$. The red shaded region represents the frequency range around the apical oxygen phonon modes, where a transient superconducting-like response could be identified. Horizontal dashed lines indicate the thermally-induced increase in $\int\sigma_1(\omega)d\omega$ when heating the sample from 100 K to 200 K (black) and the equilibrium superfluid density, $\omega\sigma_2(\omega)|_{\omega\to 0}$, measured at T = 10 K (red).

For comparison, we have also included horizontal dashed lines indicating the thermally-induced increase in $\int \sigma_1(\omega)d\omega$ when heating the sample from 100 K to 200 K (middle panel) and the equilibrium superfluid density, $\omega\sigma_2(\omega)|_{\omega\to 0}$, measured at T = 10 K (lower panel).

For excitation at the 19.2 THz discussed above and at 16.4 THz, the non-equilibrium state includes a dissipative $\int \Delta\sigma_1(\omega)d\omega$ response (analogous to that observed upon heating) that coexists with a superconducting-like imaginary conductivity ($\omega\sigma_2(\omega)|_{\omega\to 0}$) identical to that measured in the same material in the equilibrium superconducting state. However, when the pump frequency is tuned below 500 cm^{-1} (15 THz), no superconducting component is observed, whereas the dissipative response is approximately the same as that observed for $\omega_{pump} > 500$ cm^{-1}.

The different nature of the dissipative and the superconducting-like component of the signal is further underscored by the data reported in Figure 6. Here, we show the dependence of $\int \Delta\sigma_1(\omega)d\omega$ and $\omega\sigma_2(\omega)|_{\omega\to 0}$ on base temperature, for two different pump wavelengths.

The dissipative term (Fig. 5a) is temperature-independent and persists all the way up to 325 K, which suggest that its origin may be related to heating of quasiparticles.

On the other hand, the superconducting-like response (Fig. 5b), which is observed only for high-frequency pumping (blue circles), displays a strong reduction with increasing temperature, almost disappearing for T > 300 K. This is consistent with the observation reported in Refs. [5,6].

The body of evidence outlined above allows us to provide a critical assessment of the underlying mechanism for optically enhanced non-equilibrium superconductivity.

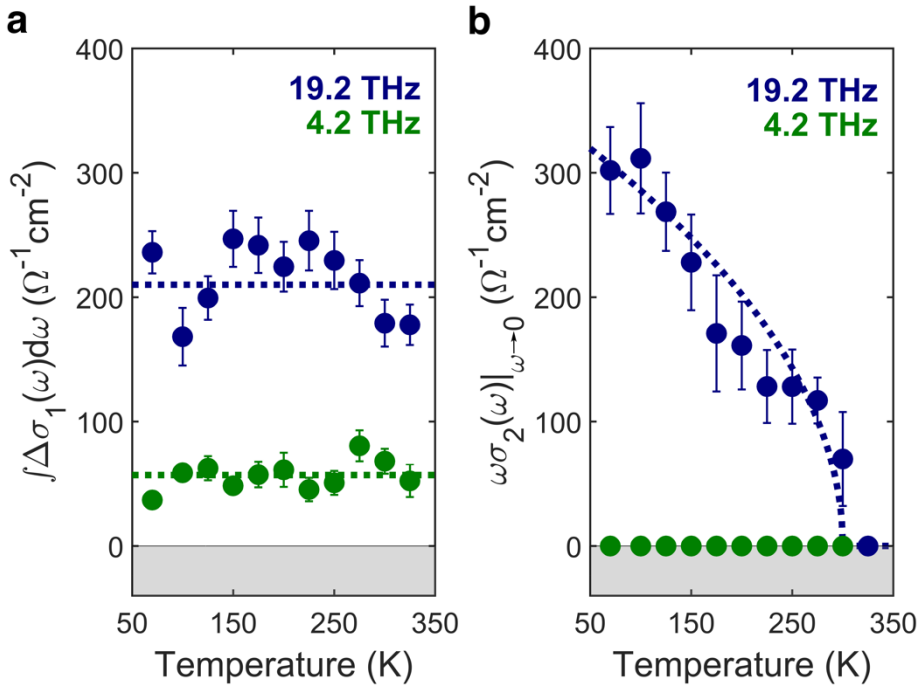

FIG. 5. Temperature dependence of the dissipative and superconducting-like responses. Temperature dependent (a) dissipative response, $\int \Delta\sigma_1(\omega)d\omega$, and (b) superconducting-like response, $\omega\sigma_2(\omega)|_{\omega\to 0}$, measured for resonant narrowband excitation of the lowest-frequency (4.2 THz) and highest-frequency (19.2 THz) phonon modes. The dashed lines are guides to the eye.

Firstly, it is clear that some form of lattice excitation must underpin optically-induced superconductivity in this frequency range. In previous studies [8,9], we have conjectured that the lowest order nonlinear lattice anharmonicity, of the type $Q_{IR}^2 Q_R$ (where Q_{IR} and Q_R are the normal coordinates of the directly driven infrared-active mode and of any anharmonically coupled Raman mode, respectively) may explain the observed phenomenology. Indeed, this lattice term leads to a transient, average structural deformation that may be beneficial to superconductivity.

The data reported in the present paper suggest that in addition to this nonlinear phononic mechanism, other phenomena may come into play. As documented in the Supplemental Material [12], when considering the calculated average lattice deformations induced by an anharmonic $Q_{IR}^2 Q_R$ coupling for each of the *IR* phonons of Figure 3, one does not find a defining feature for the two modes at 16.4 THz and

19.2 THz.

On the other hand, we stress here that these high-frequency vibrations drive large amplitude motions of the apical oxygen atoms, which are then expected to couple directly to the in-plane electronic and magnetic structure. This coupling is supposed to be much weaker for the other modes at lower frequency [13,14].

We also note that the frequency of the two apical oxygen phonons matches approximately the sum of the inter- and intra-bilayer Josephson plasma frequencies in $YBa_2Cu_3O_{6.5}$ ($\omega_{JPR,1} \simeq 1$ - 2 THz and $\omega_{JPR,2} \simeq 14$ THz, respectively). Hence, a mechanism in which driven lattice excitations couple directly to the charge and spin degrees of freedom in the planes may become resonantly enhanced at these frequencies [15,16,17,18].

Clearly, further studies that make use of the new pump device available here are needed, with special attention to measurements of time dependent lattice dynamics [9] and inelastic excitations [19,20,21]. More generally, this tuneable, spectrally-selective nonlinear pump source, applied for the first time in the present study, is expected to strongly impact the investigation of non-equilbrium phenomena in solids.

REFERENCES

[1] D. N. Basov and T. Timusk, "Electrodynamics of high-T_c superconductors," *Rev. Mod. Phys.* **77**, 721 (2005).

[2] C. C. Homes, T. Timusk, D. A. Bonn, R. Liang, and W. N. Hardy. "Optical properties along the c-axis of $YBa_2Cu_3O_{6+x}$ for $x = 0.50 \rightarrow 0.95$ Evolution of the pseudogap" *Physica C* **254**, 265-280 (1995).

[3] C. C. Homes, T. Timusk, D. A. Bonn, R. Liang, and W.N. Hardy, "Optical phonons polarized along the *c*-axis of $YBa_2Cu_3O_{6+x}$, for $x \rightarrow 0.5$ to 0.95," *Can. J. Phys.* **73**, 663 (1995).

[4] W. Hu, S. Kaiser, D. Nicoletti, C. R. Hunt, I. Gierz, M. C. Hoffmann, M. Le Tacon, T. Loew, B. Keimer, and A. Cavalleri, "Optically enhanced coherent transport in $YBa_2Cu_3O_{6.5}$ by ultrafast redistribution of interlayer coupling," *Nat. Mater*. **13**, 705 (2014).

[5] S. Kaiser, C. R. Hunt, D. Nicoletti, W. Hu, I. Gierz, H. Y. Liu, M. Le Tacon, T. Loew, D. Haug, B. Keimer, and A. Cavalleri, "Optically induced coherent transport far above T_c in underdoped $YBa_2Cu_3O_{6+\delta}$," *Phys. Rev. B* **89**, 184516 (2014).

[6] C. R. Hunt, D. Nicoletti, S. Kaiser, D. Pröpper, T. Loew, J. Porras, B. Keimer, and A. Cavalleri, "Dynamical decoherence of the light induced interlayer coupling in $YBa_2Cu_3O_{6+\delta}$," *Phys. Rev. B* **94**, 224303 (2016).

[7] M. Först, C. Manzoni, S. Kaiser, Y. Tomioka, Y. Tokura, R. Merlin, and A. Cavalleri, "Nonlinear phononics as an ultrafast route to lattice control", *Nature Physics* **7**, 854 (2011).

[8] R. Mankowsky, M. Först, T. Loew, J. Porras, B. Keimer, and A. Cavalleri, "Coherent modulation of the $YBa_2Cu_3O_{6+x}$ atomic structure by displacive stimulated ionic Raman scattering", *Phys. Rev. B* **91**, 094308 (2015).

[9] R. Mankowsky, A. Subedi, M. Först, S.O. Mariager, M. Chollet, H. Lemke, J. Robinson, J. Glownia, M. Minitti, A. Frano, M. Fechner, N. A. Spaldin, T. Loew, B. Keimer, A. Georges, and A. Cavalleri, "Nonlinear lattice dynamics as a basis for enhanced superconductivity in $YBa_2Cu_3O_{6.5}$", *Nature* **516**, 71 (2014).

[10] B. Liu, H. Bromberger, A. Cartella, T. Gebert, M. Först, A. Cavalleri, "Generation of narrowband high-intensity, carrier-envelope phase stable pulses tunable between 4 and 18 THz", *Optics Letters* **42**, 129-131 (2017).

[11] A. Cartella, T. F. Nova, A. Oriana, G. Cerullo, M. Först, C. Manzoni, and A. Cavalleri, "Narrowband carrier-envelope phase stable mid-infrared pulses at wavelengths beyond 10 µm by chirped-pulse difference frequency generation", *Optics Letters* **42**, 663-666 (2017).

[12] See Supplemental Material for details on the experimental setup, data acquisition and evaluation, fitting models, extended data sets, and the ab-initio calculations of the structural dynamics.

[13] M. Mori, G. Khalliullin, T. Tohyama, S. Maekawa, "Origin of the spatial variation of the pairing gap in Bi-based high temperature superconductors", *Phys. Rev. Lett* **101**, 24720023 (2008).

[14] Y.Y . Peng, G. Dellea, M. Conni, A. Amorese, D. Di Castro, G.M. DeLuca, K. Kummer, M. Salluzzo, X. Sun, X.J. Zhou, G. Balestino, M. LeTacon, B. Keimer, L. Braicovic, N.B. Brookes, G. Ghiringhelli "Influence of apical oxygen on the extent of the in-plane exchange interaction in cuprate superconductors" *Nature Physics* **13**, 1201 (2017).

[15] S. J. Denny, S. R. Clark, Y. Laplace, A. Cavalleri, and D. Jaksch, "Proposed Parametric Cooling of Bilayer Cuprate Superconductors by Terahertz Excitation", *Phys. Rev. Lett.* **114**, 137001 (2015).

[16] J. Okamoto, A. Cavalleri, and L. Mathey, "Theory of enhanced interlayer tunneling in optically driven high T_c superconductors", *Phys. Rev. Lett.* **117**, 227001 (2016).

[17] M. Knap, M. Babadi, G. Refael, I. Martin, and E. Demler, "Dynamical Cooper pairing in nonequilibrium electron-phonon systems", *Phys. Rev. B* **94**, 214504 (2016).

[18] M. Babadi, M. Knap, I. Martin, G. Refael, and E. Demler, "Theory of parametrically amplified electron-phonon superconductivity", *Phys. Rev. B* **96**, 014512 (2017).

[19] M. Buzzi, M. Först, R. Mankowsky, and A. Cavalleri, "Probing dynamics in quantum materials with femtosecond X-rays", *Nature Review Materials* **3**, 299-311 (2018).

[20] L. J. P. Ament, M. van Veenendaal, T. P. Devereaux, J. P. Hill, and J. van den Brink, "Resonant inelastic x-ray scattering studies of elementary excitations", *Rev. Mod. Phys.* **83**, 705 (2011).

[21] H.-H. Kim, S.M. Souliou, M. E. Barber, E. Lefrançois, M.Minola, M. Tortora, R. Heid, N. Nandi, R. A. Borzi, G. Garbarino, A. Bosak, J. Porras, T. Loew, M. König, P. J.W. Moll, A. P. Mackenzie, B. Keimer, C. W. Hicks, and M. Le Tacon, "Uniaxial pressure control of competing orders in a high-temperature superconductor", *Science* **362**, 1040-1044 (2018).

Which phonons induce non-equilibrium superconductivity in $YBa_2Cu_3O_{6.5}$?

B. Liu[1], M. Först[1], M. Fechner[1], D. Nicoletti[1], J. Porras[3], B. Keimer[3], A. Cavalleri[1,2]

[1]*Max Planck Institute for the Structure and Dynamics of Matter, Hamburg, Germany.*
[2]*Department of Physics, University of Oxford, Clarendon Laboratory, Oxford, UK*
[3]*Max Planck Institute for Solid State Research, Stuttgart, Germany.*

Supplemental Material

S1. Experimental setup

The optical setup used to photo-excite $YBa_2Cu_3O_{6.5}$ with tunable narrowband pump pulses and to probe its low-frequency THz response is sketched in Figure S1. It was fed by a 1-kHz repetition rate Ti:sapphire regenerative amplifier, delivering 7-mJ, 80-fs pulses at 800 nm wavelength.

We used 90% of the pulse energy to generate the excitation pulses. To this end, we pumped two parallel home-built optical parametric amplifiers (OPA), which were seeded with the same white light to produce carrier-envelope-phase (CEP) stable THz pump pulses in a subsequent difference frequency generation (DFG) process [1,2]. The two OPA signal outputs of ~120 fs duration were directly sent to a 1-mm thick GaSe crystal to generate the broadband pump pulses at 19.2 THz with relative bandwidth $\Delta\nu/\nu \sim 20\%$. For the generation of narrowband pulses with relative bandwidth $\Delta\nu/\nu < 10\%$, the two signal outputs were linearly chirped to a pulse duration of ~600 fs before the DFG process in either a 0.5 mm thick DSTMS organic crystal [3] or in the same 1-mm GaSe crystal. The pulse energies achieved were always at the few-μJ level. The maximum peak electric fields of the focused beams at the sample surface were 2.9 and 2.7 MV/cm for 4.2 and 10 THz, respectively, and about 3.1 MV/cm for both 16.4 and 19.2 THz pulses. They could be attenuated by inserting a pair of free-standing wire grid polarizers.

Single-cycle THz probe pulses with spectral components between 10 cm^{-1} and 80 cm^{-1} were generated via optical rectification of 500-μJ pulses at the fundamental 800 nm wavelength in a 0.5 mm thick ZnTe crystal.

The experiments were performed on the *ac* surface (~2 × 0.5 mm^2) of a $YBa_2Cu_3O_{6.5}$ single crystal. A sharp superconducting transition at $T_C = 52$ K was determined by dc

magnetization measurements [4]. Both pump and probe beams were polarized along the crystallographic *c* axis. The THz electric field of the probe pulses reflected from the sample surface was detected via electro-optic sampling in a 500-μm thick optically contacted ZnTe crystal.

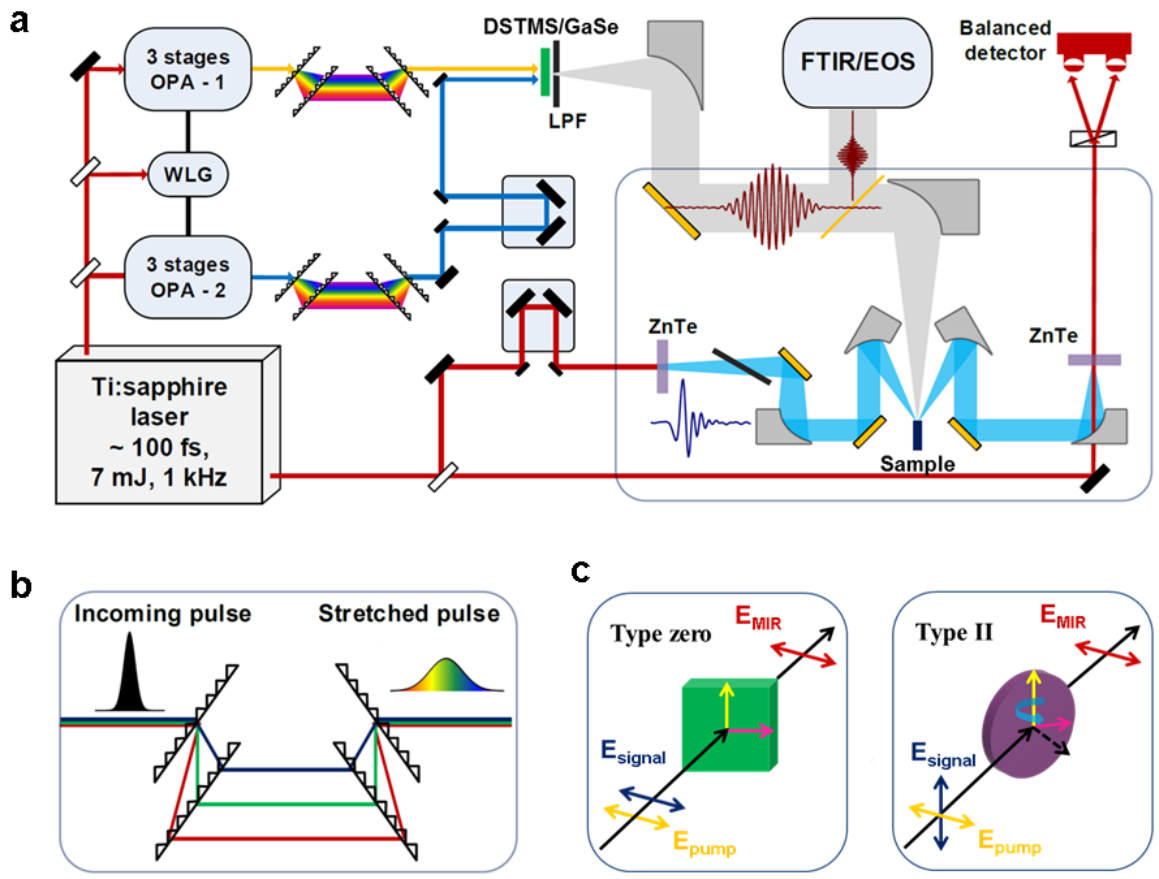

Figure S1. a. Narrowband THz pump / THz probe setup. OPA, optical parametric amplifier. WLG, white light generation. LPF, long-pass filter. Two near-infrared signal outputs from two parallel OPAs were linearly chirped and sent to a nonlinear crystal (DSTMS/GaSe) for difference frequency generation (DFG). The generated pump pulses were separated from the near-infrared inputs and characterized by either Fourier-transform spectroscopy (FTIR) or electro-optic sampling (EOS). These pump pulses were set to be polarized along the *c* axis of $YBa_2Cu_3O_{6.5}$, with their frequency tuned to be resonant with different phonon modes. The transient optical properties were measured by detecting the THz electric field generated from a ZnTe crystal via optical rectification and reflected from the sample surface, as a function of pump-probe time delay. **b.** Pulse stretcher consisting of four transmission gratings. **c.** Phase-matching condition and DFG process in DSTMS (left) and GaSe (right) crystals.

S2. Data acquisition and evaluation

Time-domain THz spectroscopy was used to characterize the transient response of $YBa_2Cu_3O_{6.5}$ induced by optical driving. The spectral response at each time delay after excitation was obtained by keeping fixed the delay τ between the pump pulse and the electro-optic sampling gate pulse, and scanning the single-cycle THz probe pulse with internal delay *t* across.

The stationary probe electric field $E_R(t)$ and the differential electric field $\Delta E_R(t,\tau)$ reflected from the sample were recorded simultaneously by feeding the electro-optic sampling signal into two lock-in amplifiers and mechanically chopping the pump and probe beams at different frequencies of ~357 and 500 Hz, respectively. The differential signal $\Delta E_R(t,\tau)$ was sampled at the ~143 Hz difference frequency of the two choppers. This approach minimized the cross-talk between the two detected signals whilst reducing the noise level of the measurements.

The electric field $E_R(t)$ and the differential field $\Delta E_R(t,\tau)$ were independently Fourier transformed to obtain the complex-valued, frequency-dependent $\tilde{E}_R(\omega)$ and $\Delta\tilde{E}_R(\omega,\tau)$. The photo-excited complex reflection coefficient $\tilde{r}(\omega,\tau)$ was determined by [5,6]

$$\frac{\Delta\tilde{E}_R(\omega,\tau)}{\tilde{E}_R(\omega)} = \frac{\tilde{r}(\omega,\tau) - \tilde{r}_0(\omega)}{\tilde{r}_0(\omega)},$$

where $\tilde{r}_0(\omega)$ is the stationary reflection coefficient known from the equilibrium optical response.

The penetration depth of the excitation pulses is a factor of ~2-10 smaller than that of the low-frequency THz probe pulses, implying that we were not probing a homogeneously excited sample volume. This mismatch was considered in the data analysis. At each

frequency, the penetration depths of the electric fields into the material were calculated by $d(\omega) = \frac{c}{2\omega \cdot \mathrm{Im}[\tilde{n}_0(\omega)]}$ (here $\tilde{n}_0(\omega)$ is the stationary complex refractive index), yielding values of ~10–20 μm for the THz probe and in the range of ~1-5 μm for the pump pulses.

An accurate estimate of the photo-induced optical response functions was then achieved by treating the sample as a multi-layer system, in which only a thin layer below the sample surface is homogeneously excited while the bulk layer below remains unperturbed. The complex reflection coefficient is then expressed as

$$\tilde{\mathrm{r}}(\omega,\tau) = \frac{\tilde{\mathrm{r}}_A(\omega,\tau) + \tilde{\mathrm{r}}_B(\omega)e^{2i\delta(\omega,\tau)}}{1 + \tilde{\mathrm{r}}_A(\omega,\tau)\tilde{\mathrm{r}}_B(\omega)e^{2i\delta(\omega,\tau)}}$$

Here, $\tilde{\mathrm{r}}_A(\omega,\tau)$ and $\tilde{\mathrm{r}}_B(\omega,\tau)$ are the reflection coefficients at the interfaces vacuum/photoexcited layer and photoexcited layer/unperturbed bulk, respectively, while $\delta = 2\pi d\tilde{n}(\omega,\tau)/\lambda_0$, with $\tilde{n}(\omega,\tau)$ being the complex refractive index of the photo-excited layer and λ_0 the probe wavelength.

Numerically solving this equation allowed us to retrieve $\tilde{n}(\omega,\tau)$ from the reflection coefficient $\tilde{\mathrm{r}}(\omega,\tau)$ obtained in the experiment. The complex optical conductivity for the homogeneously excited volume of the material is expressed as $\tilde{\sigma}(\omega,\tau) = \frac{\omega}{4\pi i}[\tilde{n}(\omega,\tau)^2 - \varepsilon_\infty]$, with $\varepsilon_\infty = 4.5$ as a standard value for high-T_C cuprates.

S3. Fitting models

At each pump probe time delay τ, the transient *c*-axis optical response functions were fitted either with a model including the response of a Josephson plasma or with a simple Drude-Lorentz model for normal conductors [6]. A single set of fit parameters was always

used to simultaneously reproduce the real and imaginary part of the optical conductivity, $\sigma_1(\omega)$ and $\sigma_2(\omega)$.

The phonon modes in the mid-infrared (150 cm$^{-1} \lesssim \omega \lesssim$ 700 cm^{-1}) and the high-frequency electronic absorption ($\omega \gtrsim$ 3000 cm $^{-1}$) were constructed by fitting the equilibrium spectra with Lorentz oscillators, for which the complex dielectric function is expressed as:

$$\tilde{\varepsilon}_{HF}(\omega) = \sum_i \frac{S_i^2}{(\Omega_i^2 - \omega^2) - i\omega\Gamma_i}.$$

Here, Ω_i, S_i, and Γ_i are the central frequency, strength, and damping coefficient of the *i*-th oscillator, respectively. In all fitting procedures to the transient data, these high-frequency terms were kept fixed.

The low-frequency Drude contribution to the complex dielectric function is expressed as

$$\tilde{\varepsilon}_D(\omega) = \varepsilon_\infty[1 - \omega_P^2/(\omega^2 + i\Gamma\omega)],$$

where ω_P and Γ are the Drude plasma frequency and momentum relaxation rate, which were left as free fitting parameters, while ε_∞ was kept fixed to 4.5.

The dielectric function of the Josephson plasma is expressed instead as

$$\tilde{\varepsilon}_J(\omega) = \varepsilon_\infty\left(1 - \omega_J^2/\omega^2\right) + \tilde{\varepsilon}_N(\omega).$$

Here, the free fitting parameters are the Josephson plasma frequency, ω_J, and $\tilde{\varepsilon}_N(\omega)$, a weak "normal fluid" component [6,7] (overdamped Drude term), which was introduced to reproduce the positive offset in $\sigma_1(\omega)$.

As an example, the photo-induced optical conductivity for 19.2 THz narrowband excitation at different time delays τ = 0.6 ps and 2.4 ps and the corresponding fits are reported in Figure S3. At early time delay (τ = 0.6 ps), the Josephson plasma model (black

solid lines) is able to reproduce the experimental data. Notably, a Drude response alone (dashed lines) would not capture the measured low-frequency increase in $\sigma_2(\omega)$.

At later time delays (Fig. S3b), for which the system has already evolved into a dissipative response, the experimental data could instead be well reproduced by the simple Drude model for normal conductors.

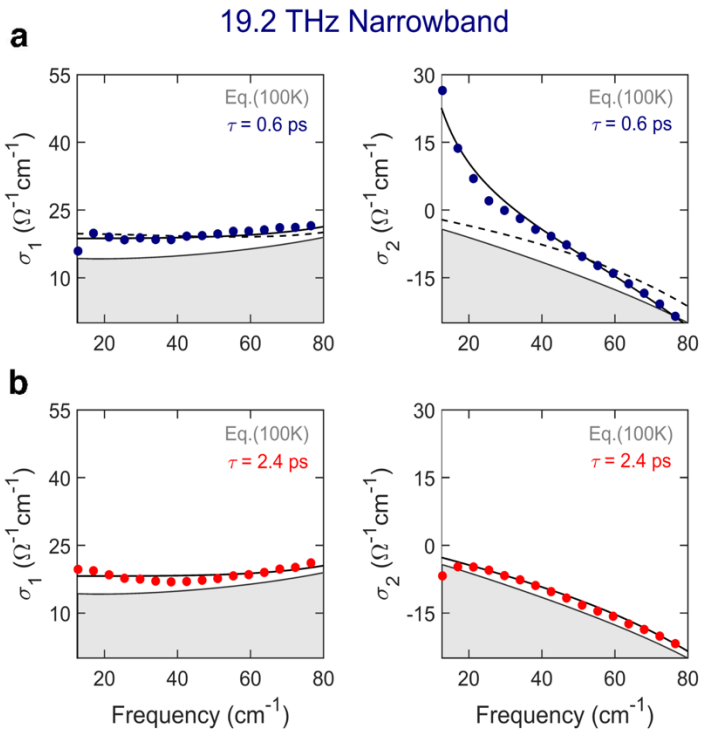

Figure S3. Fits to the transient complex optical conductivity measured after narrowband excitation at ω_{pump} = 19.2 THz (T = 100 K). **a.** Real and imaginary part of the optical conductivity measured at τ = 0.6 ps pump-probe time delay (blue dots). Grey curves with shading are the corresponding equilibrium spectra (shown also in panels b). The black solid line is a fit with the Josephson plasma model. The dashed black curve is instead a failed fit attempt using a simple Drude term for normal conductors. **b.** Real and imaginary conductivity measured at τ = 2.4 ps time delay (red dots). This dissipative response could be well reproduced by the Drude-Lorentz model (black solid lines).

S4. Extended data sets

The full dynamical evolution of the photoinduced changes in the complex optical conductivity at $T = 100\ K \gg T_C$, which is reported in Fig. 2 of the main text for both

broadband and narrowband excitation at $\omega_{pump} = 19.2$ THz, is shown here also for narrowband excitation at $\omega_{pump} = 16.4$ THz (Fig. S4.1), $\omega_{pump} = 4.2$ THz, and $\omega_{pump} = 10.1$ THz (Fig. S4.2).

For each data set, we display color plots of the real and imaginary part of the optical conductivity as a function of both frequency and pump-probe time delay, along with selected spectra measured at the peak of the response (see also Fig. 3 in main text). In addition, we plot two frequency-integrated quantities, as a function of time delay: $\omega\sigma_2(\omega)|_{\omega\to 0}$, which in a superconductor is proportional to the superfluid density, and $\int \Delta\sigma_1(\omega)d\omega$, which is a reporter of dissipation and quasiparticle heating inside the gap.

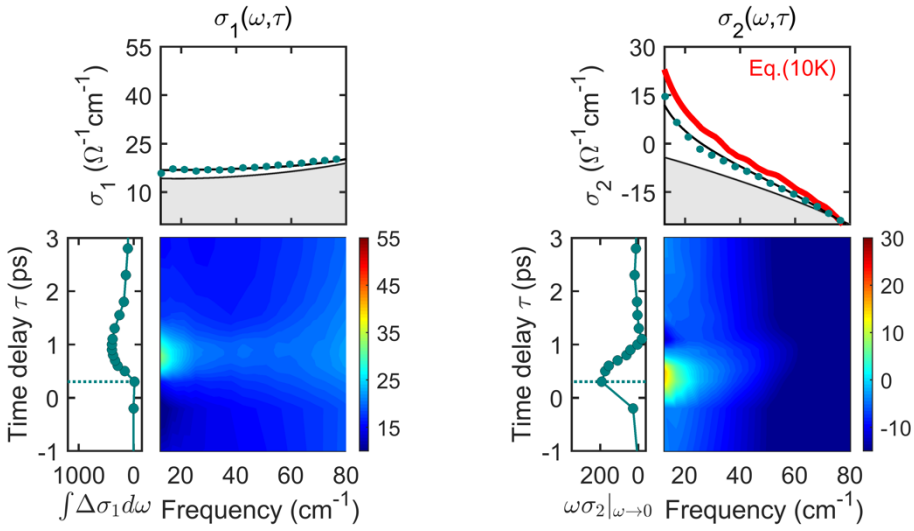

Figure S4.1. Frequency- and time-delay-dependent complex optical conductivity measured at T = 100 K for narrowband excitation at 16.4 THz (color plots). Upper panels: corresponding $\sigma_1(\omega)$ and $\sigma_2(\omega)$ line cuts displayed at equilibrium (grey lines) and at the time delay corresponding to the peak of the coherent response (teal circles). Black lines are fits to the transient spectra with a model describing the response of a Josephson plasma. For comparison, we also report the equilibrium $\sigma_2(\omega)$ measured in the superconducting state at T = 10 K (red line). Side panels: Frequency-integrated dissipative ($\int \Delta\sigma_1(\omega)d\omega$) and coherent ($\omega\sigma_2(\omega)|_{\omega\to 0}$) responses, as a function of pump-probe time delay. The delay corresponding to the spectra reported in the upper panels is indicated by a dashed line.

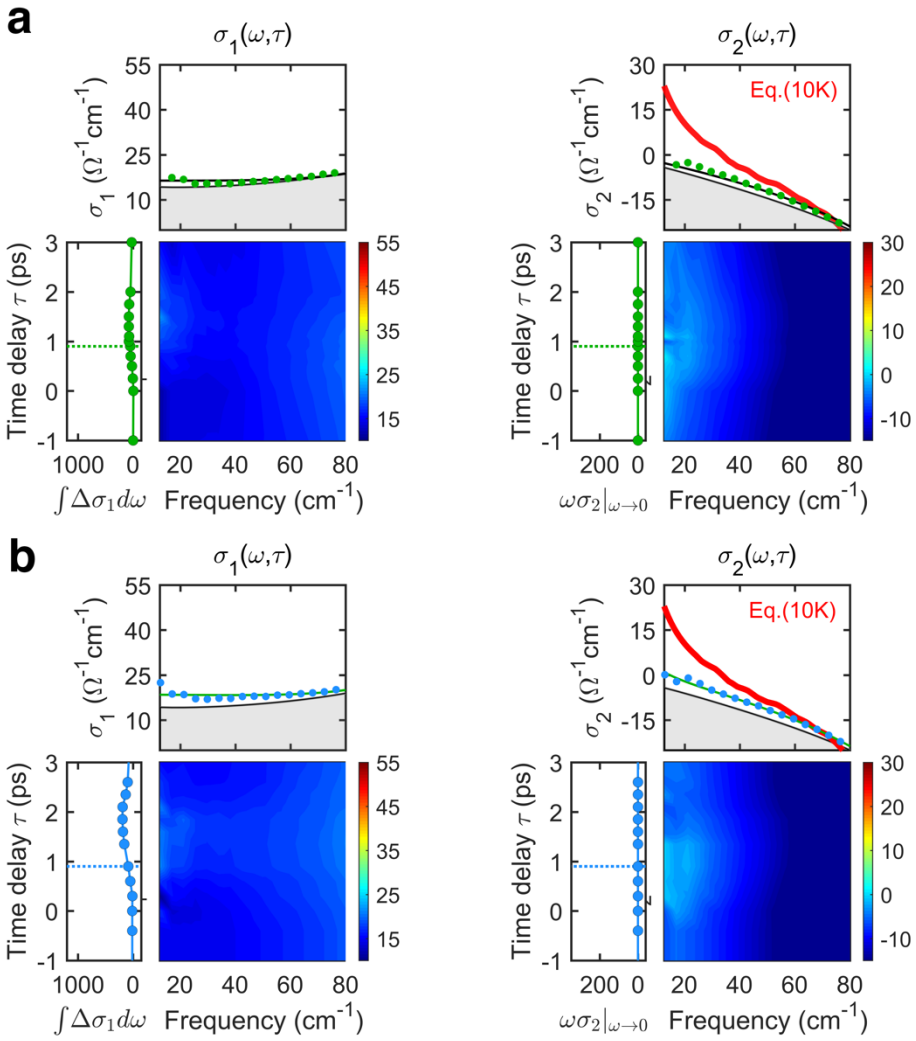

Figure S4.2. **a,** Frequency- and time-delay-dependent complext optical conductivity measured at T = 100 K for narrowband excitation at 4.2 THz (color plots). Upper panels: corresponding $\sigma_1(\omega)$ and $\sigma_2(\omega)$ line cuts displayed at equilibrium (grey lines) and at the time delay corresponding to the peak of the response (green circles). Black lines are fits to the transient spectra with a Drude-Lorentz model. For comparison, we also report the equilibrium $\sigma_2(\omega)$ measured in the superconducting state at T = 10 K (red line). Side panels: Frequency-integrated dissipative ($\int \Delta\sigma_1(\omega)d\omega$) and coherent ($\omega\sigma_2(\omega)|_{\omega\to 0}$) responses, as a function of pump-probe time delay. The delay corresponding to the spectra reported in the upper panels is indicated by a dashed line. **b,** Same quantities as in **a,** measured for narrowband excitation at 10.1 THz.

As already extensively discussed in the main text, only driving at the two highest frequencies modes (ω_{pump} = 16.4 THz and ω_{pump} = 19.2 THz) induced a superconducting-like response ($\sigma_2(\omega) \propto 1/\omega$), for which the transient complex conductivity was fitted by a model describing the optical response of a Josephson plasma.

On the other hand, excitation of the two low-frequency modes (ω_{pump} =4.2 THz and ω_{pump} =10.1 THz) caused a moderate increase in dissipation and no superconducting component. This observation could be well reproduced, for all time delays, by a simple Drude-Lorentz model for normal conductors.

S5. Ab-initio calculations of the structural dynamics

In this Section, we correlate the experimentally-determined frequency band for the stimulation of transient superconductivity with the optically-driven rearrangement of the crystal structure, which we calculated by combining effective Hamiltonian modeling with first-principle computations.

Our approach is based on an anharmonic crystal potential that consists of three distinct contributions [8,9,10]:

1. The harmonic potential of each phonon mode

$$V_{harm} = \sum \frac{\omega_i^2}{2} Q_i^2, \tag{S5.1}$$

with ω_i and Q_i representing the eigenfrequency and coordinate of the i-th mode, respectively.

2. The anharmonic potential containing higher-order terms of the phonon coordinates and combinations of different phonon modes

$$V_{anharm} = \sum g_{ijk} Q_i Q_j Q_k + \sum f_{iklm} Q_i Q_k Q_l Q_m, \tag{S5.2}$$

with g_{ijk} and f_{iklm} indicating third and fourth order anharmonic coefficients, respectively.

3. The coupling of each individual phonon mode to an external electric field

$$V_{efield} = \sum Z_i^* Q_i E_{field} \,, \tag{S5.3}$$

with Z_i^* representing the mode effective charge [11,12].

The structural dynamics are then determined by the equations of motion for each phonon mode, given by

$$\ddot{Q}_i + 2\gamma_i \dot{Q}_i + \nabla_{Q_i}\left(V_{harm} + V_{anharm} + V_{efield}\right) = 0. \tag{S5.4}$$

Here, we introduced a phenomenological damping term γ_i, which accounts for contributions to the finite lifetime which are not already considered within the anharmonic potential. Importantly, the equations are restricted to phonon modes at the Brillouin zone center, due to the long wavelengths of the THz excitation pulses.

Various studies have shown that this approach is able to describe the structural dynamics induced by the resonant excitation of infrared-active modes in a solid [13,14]. However, only a small subset of all possible phonon coupling constants was considered in these cases, predominantly due to computational limitations. In the present simulations, this reduction was overcome by utilizing the approaches given in Refs. [8,15]. We list all technical and numerical details at the end of this Section.

We simulated the THz-driven structural dynamics of the ortho-II structure of $YBa_2Cu_3O_{6.5}$, which exhibits 73 non-translational phonon modes at the Brillouin zone center. The most relevant phonon modes for *c*-axis polarized THz excitation are 13 B_{1u} modes, which exhibit a finite electric dipolar moment along this direction. In addition, there are 11 A_g modes, which fulfill the symmetry requirements to exhibit a finite third-order type coupling to the B_{1u} modes [8,13]. A full list of the eigenfrequencies of these modes is presented at the end of this Section.

The calculated effective charges for the B_{1u} modes, needed to describe their excitation by a THz electric field according to Eq. (S5.3), are shown in Figure S5.1a. We assumed here that the Born effective charge of each atom equals its ionic charge. In agreement with experimental observations [16], we obtain large values for the two highest-frequency apical-oxygen modes at 16.5 THz and 20.5 THz, for the 10-THz mode affecting the CuO_2 layers, and for the mode at 4 THz that involves Ba displacements. Note also that all phonon frequencies match within a few percent the values determined from the experiment.

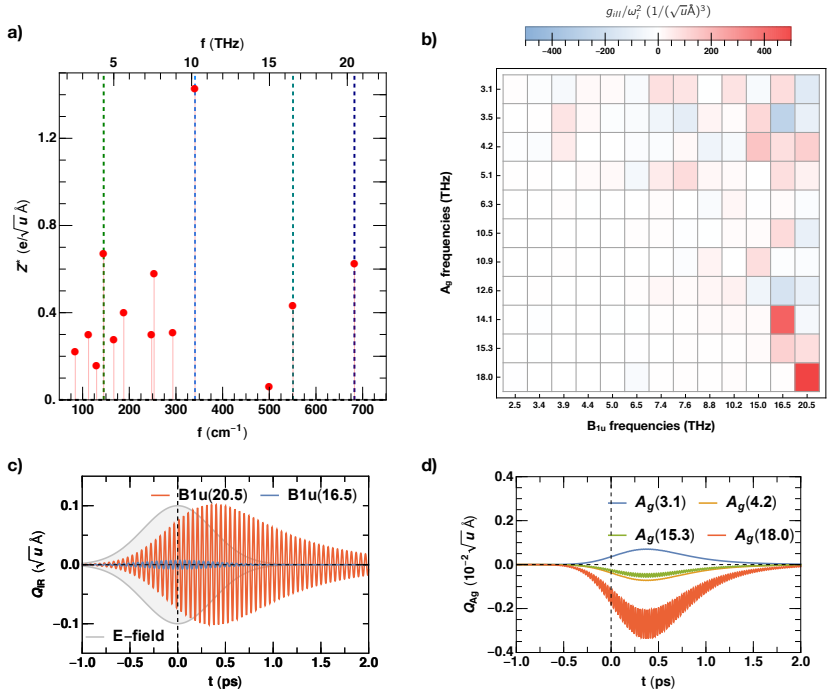

Figure S5.1. **a** Mode effective charges for the polar B_{1u} modes of the $YBa_2Cu_3O_{6.5}$ ortho-II structure. **b** Third-order anharmonic coupling coefficients of the type $Q_{Ag}Q_{IR}^2$ for all B_{1u} and A_g modes. **c** Oscillations of two B_{1u} modes at 16.5 and 20.5 THz driven by a narrowband THz pulse at 20.5 THz (grey area). **d** Dynamics of the four A_g modes exhibiting stronger coupling to the 20.5-THz B_{1u} mode driven in panel c.

Group symmetry dictates three sets of third-order couplings for the phonon modes considered. The first is the coupling of the square of the optically-excited B_{1u} modes to a single A_{1g} mode, proportional to $Q_{IR,i}^2 Q_{Ag}$. The second is the coupling of two different B_{1u}

modes to a single A_{1g} mode ($Q_{IR,i}Q_{IR,j}Q_{Ag}$), and the third is the coupling between three A_{1g} modes ($Q_{Ag,i}Q_{Ag,j}Q_{Ag,k}$). For the fourth-order coupling terms, we only considered the terms of the form Q_i^4 and neglected expressions mixing two or more phonon modes. Thus, we took into account, in total, 1067 third-order and 24 fourth-order coupling coefficients. Note that, in the earlier studies of Refs. [8,13], at maximum 24 coupling coefficients were considered. As an example, Figure S5.1b shows a subset of the computed anharmonic coupling coefficients, representing the two-mode coupling of the type $Q_{IR,i}^2 Q_{Ag}$. Both the two highest-frequency B_{1u} polar modes couple strongly to two different A_{1g} modes, similar to the observations reported for $YBa_2Cu_3O_7$ in Ref. [8].

Figure S5.1c,d show the dynamics of two selected B_{1u} modes and four anharmonically coupled A_g modes. The time traces have been triggered by an electric field pulse $E(t) = e^{\frac{2t^2 ln(2)}{FWHM^2}} cos(\omega t)$ with a 3 MV/cm peak field and 0.6 ps pulse duration (FWHM) at 20.5 THz. The resonantly excited 20.5-THz B_{1u} mode oscillates with an amplitude that is about one order of magnitude larger than that of the off-resonant B_{1u} mode at 16.5 THz. The dominant A_g modes, anharmonically coupled to the B_{1u} phonons, are transiently displaced from their equilibrium positions with significant amplitudes ($|Q_{Ag}| < 10^{-5}\sqrt{u}$Å). They reach their maximum displacements at about 0.4 ps time delay, for which also the resonantly driven 20.5-THz B_{1u} mode reaches its peak amplitude.

In the same way, we constructed the time dependent crystal structures for different excitation frequencies between 2.5 and 22 THz and focused on the transient displacements of A_g modes, which involve an average distortion of the crystal lattice [8,13]. Figure S5.2 shows the maximum changes of selected bonds (distance of the apical oxygen atoms from the CuO_2 planes, inter-bilayer distance of the CuO_2 planes, and buckling of the CuO_2 planes) calculated from these average phonon displacements. Peak

electric field and pulse duration were kept fixed at 3 MV/cm and 0.6 ps, respectively, for all driving frequencies.

For excitation in the interval between 5 and 10 THz, we observed a significant shift of the apical oxygen atoms closer to the CuO_2 planes, accompanied by a buckling within the CuO_2 layers and an increase in the intra-bilayer distance. In contrast, very different rearrangements were found for driving frequencies within the range for which photo-induced superconducting coherence was observed. Most prominently, the apical oxygen atoms moved away from the CuO_2 planes for resonant driving of the 20.5-THz phonon, while excitation of the 16.5-THz mode shifted them atoms closer to the planes. In both cases, we also calculated different signs for the CuO_2 plane buckling and the intra-bilayer distance, which increased for 16.5-THz but decreased for the 20.5-THz excitation.

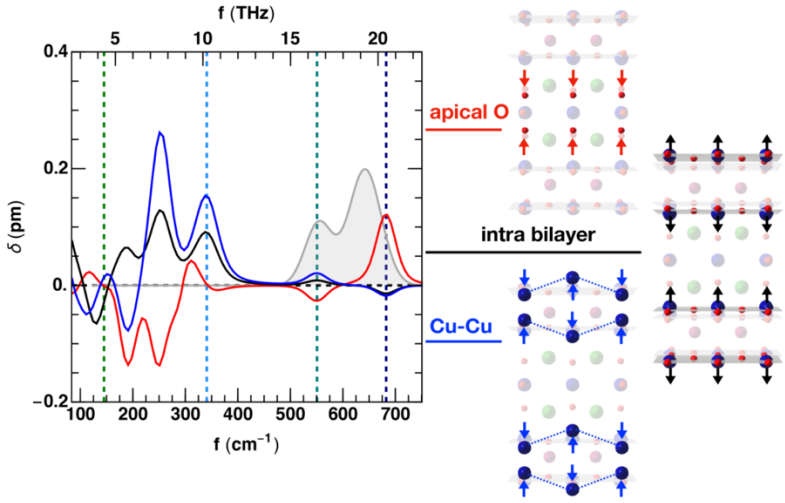

Figure S5.2. Transient average distortions of the apical oxygen positions (red), the intra-bilayer distance (black) and the planar Cu buckling (blue) in $YBa_2Cu_3O_{6.5}$, derived from ab-initio calculations of nonlinear phonon-phonon interactions for different excitation frequencies. The grey shaded area depicts the experimentally determined frequency range of the optically-enhanced superconducting response shown in Figure 4 of the main text. The excitation parameters of 600 fs pulse duration and 3 MV/cm peak electric field, used in the calculations, reproduce the experimental conditions. Arrows in the illustrations shown on the right correspond to positive displacements.

Overall, we did not find a consistent trend in the transient crystal structures, which was unique to the frequency band for which transient superconductivity was observed. As such, this result puts some doubts on the significance of anharmonic phonon coupling as a possible mechanism for optically-driven superconductivity in $YBa_2Cu_3O_{6+x}$, as posited earlier in Ref. [13].

Technical and numerical approach:

We employed first-principles total energy calculations in the framework of the density functional theory (DFT) to compute all harmonic and anharmonic terms included in the equations (S5.1), (S5.2), and (S5.3). Specifically, we used the implantation of DFT, applying the linearized augmented-plane wave method (LAPW) within the ELK-code [17]. We approximated the exchange-correlation functional by the local density approximation. In addition, we performed careful tests of all relevant numerical parameters entering the computation. The setting for well-converged results corresponded to a truncation at l_{max}=10 of the angular expansion of wave functions and potential within the muffin-tin radii (2.6, 2.8, 1.85 and 1.4 a.u. for Y, Ba, Cu, and O, respectively). A $|G|_{max}$=20 a.u.$^{-1}$ limited the potential and density expansion within the interstitial region. We set $R_{MT} \times k_{max}$=8.0 for truncating the plane-wave wavefunction expansion. The Brillouin zone was sampled within our computations by a 11×19×5 k-point mesh. The same configuration was also employed in a previous study [18] and, within this setting, the forces (most relevant for phonons and anharmonic terms) were made to converge by less than 0.1 meV/Å.

Before computing the coefficients of the anharmonic potential, we first structurally relaxed the unit cell of $YBa_2Cu_3O_{6.5}$, for which we considered the ortho-II structure,

following previous studies and the experimental setting [13]. As lowest energy state, we obtained the atomic configuration given in Table S5.1.

Table S5.1. DFT minimized structural configuration of the $YBa_2Cu_3O_{6.5}$ ortho-II cell with $a = 7.55$ Å, $b = 3.81$ Å, and $c = 11.50$ Å.

element	Wykoff position	*x*	*z*	element	Wykoff position	*X*	*z*
Y	l	0.251	0.500	O1	e	0.000	0.000
Ba	x	0.244	0.187	O2	w	0.250	0.378
Cu1	a	0.000	0.000	O3	r	0.000	0.378
Cu2	b	0.500	0.000	O4	t	0.500	0.378
Cu3	q	0.000	0.356	O5	q	0.000	0.161
Cu4	s	0.500	0.355	O6	s	0.500	0.153

Table S5.2. Computed DFT eigenfrequencies of the phonon modes at the center of the Brillouin zone for the $YBa_2Cu_3O_{6.5}$ ortho-II structure.

Label	f (THz)	Label	f (THz)	Label	f (THz)	Label	f (THz)
A_g	3.1	B_{1u}	7.4	B_{2u}	17.0	B_{3u}	8.1
A_g	3.5	B_{1u}	7.6	B_{2u}	17.4	B_{3u}	8.4
A_g	4.2	B_{1u}	8.8	B_{2g}	1.8	B_{3u}	10.3
A_g	5.1	B_{1u}	10.2	B_{2g}	2.6	B_{3u}	10.5
A_g	6.3	B_{1u}	15.0	B_{2g}	4.1	B_{3u}	11.8
A_g	10.5	B_{1u}	16.5	B_{2g}	4.2	B_{3u}	13.4
A_g	10.9	B_{1u}	20.5	B_{2g}	6.5	B_{3u}	18.3
A_g	12.6	B_{1g}	2.9	B_{2g}	7.4	B_{3g}	2.0
A_g	14.1	B_{1g}	3.8	B_{2g}	8.7	B_{3g}	4.1
A_g	15.3	B_{1g}	9.7	B_{2g}	10.0	B_{3g}	5.4
A_g	18.0	B_{2u}	2.4	B_{2g}	11.3	B_{3g}	6.5
A_u	2.8	B_{2u}	3.6	B_{2g}	11.4	B_{3g}	10.3
A_u	10.8	B_{2u}	4.7	B_{2g}	18.1	B_{3g}	11.1
B_{1u}	2.5	B_{2u}	5.2	B_{3u}	2.5	B_{3g}	16.6
B_{1u}	3.4	B_{2u}	5.6	B_{3u}	2.9	B_{3g}	17.2
B_{1u}	3.9	B_{2u}	8.0	B_{3u}	3.7		
B_{1u}	4.4	B_{2u}	10.3	B_{3u}	3.8		
B_{1u}	5.0	B_{2u}	11.5	B_{3u}	4.7		
B_{1u}	5.6	B_{2u}	16.6	B_{3u}	5.4		

Finally, the phonon eigensystem was computed by frozen-phonon calculation using symmetry-adapted distortions generated with the Phonopy package [19]. We list all modes at the zone center in Table S5.2. Next, we applied the prescription in Ref. [15] to calculate the anharmonic constants of third order and took the approach of Ref. [8] for the quartic order terms.

Last, we computed the mode-effective charges appearing in equation (S5.3) by using the nominal averaged ionic charges of each atom as Born charges. Explicitly, we have for Yttrium 3+, Barium 2+, Copper 2+ and Oxygen 2-.

References (Supplemental Material)

[1] A. Sell, A. Leitenstorfer, and R. Huber, Opt. Lett. **33**, 2767 (2008).

[2] C. Manzoni, H. Ehrke, M. Först, and A. Cavalleri, Opt. Lett. **35**, 757 (2010).

[3] B. Liu, H. Bromberger, A. Cartella, T. Gebert, M. Först, and A. Cavalleri, Opt. Lett, **42**, 129 (2017).

[4] W. Hu, S. Kaiser, D. Nicoletti, C. R. Hunt, I. Gierz, M. C. Hoffmann, M. Le Tacon, T. Loew, B. Keimer, and A. Cavalleri, Nat. Mater. **13**, 705 (2014).

[5] S. Kaiser, C. R. Hunt, D. Nicoletti, W. Hu, I. Gierz, H. Y. Liu, M. Le Tacon, T. Loew, D. Haug, B. Keimer, and A. Cavalleri, Phys. Rev. B **89**, 184516 (2014).

[6] D. Nicoletti, D. Fu, O. Mehio, S. Moore, A. S. Disa, G. D. Gu, and A. Cavalleri, Phys. Rev. Lett. **121**, 267003 (2018).

[7] D. van der Marel and A. Tsvetkov, Czech. J. Phys. **46**, 3165 (1996).

[8] M. Fechner and N. A. Spaldin, Phys. Rev. B **94**, 134307 (2016).

[9] A. Subedi, A. Cavalleri, and A. Georges, Phys. Rev. B **89**, 220301 (2014).

[10] D. M. Juraschek, M. Fechner, and N. A. Spaldin, Phys. Rev. Lett. **118**, 054101 (2017).

[11] X. Gonze and C. Lee, Phys. Rev. B **55**, 10355 (1997).

[12] A. Cartella, T. F. Nova, M. Fechner, R. Merlin, and A. Cavalleri, Proc. Natl. Acad. Sci. USA **115**, 12148 (2018).

[13] R. Mankowsky, A. Subedi, M. Först, S. O. Mariager, M. Chollet, H. T. Lemke, J. S. Robinson, J. M. Glownia, M. P. Minitti, A. Frano, M. Fechner, N. A. Spaldin, T. Loew, B. Keimer, A. Georges, and A. Cavalleri, Nature **516**, 71 (2014).

[14] M. Kozina, M. Fechner, P. Marsik, T. van Driel, J. M. Glownia, C. Bernhard, M. Radovic, D. Zhu, S. Bonetti, U. Staub, and M. C. Hoffmann, Nat. Phys. **15**, 387 (2019).

[15] G. Khalsa and N. A. Benedek, Npj Quantum Mater. **3**, 15 (2018).

[16] C. C. Homes, T. Timusk, D. A. Bonn, R. Liang, and W. N. Hardy, Can. J. Phys. **675**, 663 (1995).

[17] http://elk.sourceforge.net, (n.d.).

[18] R. Mankowsky, M. Fechner, M. Först, A. von Hoegen, J. Porras, T. Loew, G. L. Dakovski, M. Seaberg, S. Möller, G. Coslovich, B. Keimer, S. S. Dhesi, and A. Cavalleri, Struct. Dyn. **4**, 044007 (2017).

[19] A. Togo and I. Tanaka, Scr. Mater. **108**, 1 (2015).